

01,15

Gas bubble evolution in Ni, Cu, W and 316 under annealing: a comparison of theory and experiment

© A.M. Ovcharenko

National Research Center „Kurchatov Institute“,
Moscow, Russia

E-mail: Ovcharenko_AM@nrcki.ru, nrcki@nrcki.ru

Received February 16, 2025

Revised March 18, 2025

Accepted March 19, 2025

A theoretical study of evolution of mono- and diatomic gas bubbles in metals driven by the Ostwald ripening mechanism under annealing at earlier and later coarsening stages is carried out. Results of the study are compared with known experimental annealing data in metals and alloys pre-implanted with helium. A comparative analysis is undertaken to assess materials that serve as structural elements in both fission and fusion reactors. Temperature dependencies for the bubble radius and density correspond closely with observed measurements. Ostwald ripening is presumably the most probable mechanism of gas bubble evolution in annealed materials taken for consideration.

Keywords: bubble coarsening, annealing, implantation, Ostwald ripening, helium, hydrogen, irradiated metals.

DOI: 10.61011/PSS.2025.03.60869.34-25

1. Introduction

Helium atoms result from threshold transmutation reactions (n, α) in structural materials of nuclear fission and fusion reactors. Helium is produced by neutrons mainly on Ni and Cu [1]. An increased helium and hydrogen production on Fe in fusion reactors is also observed [2]. It is also known that helium enters nuclear fusion reactor materials irradiated by ~ 3.5 MeV α -particles [3] and as a result of tritium accumulation in metals followed by radioactive decay.

Helium and hydrogen facilitate the generation and growth of cavities in metals and alloys irradiated in the homologous temperature range from $0.3T_m$ to $0.5T_m$, where T_m is the melting temperature. At high temperatures, $> 0.5T_m$, a thermal vacancy flux might be significant and, together with gas atom transport, affect the bubble accumulation due to the edge dislocation climb in metals and vacancy emission by grain boundaries. This gives rise to the modification of physical and mechanical properties of structural materials of nuclear fission and fusion reactors, which is of great scientific and practical interest.

Currently known research data concerning the generation and properties of gas porosity was to a large extent obtained during experimental studies of pre-implanted gas followed by material annealing [4,5]. Implantation of helium and hydrogen ions into metal is used to simulate nuclear and nuclear fusion reactor materials in high-temperature plasma conditions. Also, gas diffusion properties taken from such experiments make it possible to perform physically-based modelling of bubble growth in metallic materials.

Study of the bubble evolution during annealing in metals saturated with gas impurities addresses two potential bubble growth mechanisms: Brownian motion and coalescence (BMC) [6] and Ostwald ripening (OR) [7]. Despite the

fact that both mechanisms have been known for years, it is not clearly understood which of them is more preferable. For example, in [8], theoretical time dependences obtained using the BMC model were successfully confirmed by numerical calculation data and by comparison with the bubble accumulation data for P7 austenitic alloy. On the other hand, a new theoretical approach was proposed to the study of bubble evolution according to the OR mechanism [9]. The proposed time dependences provided good description of helium bubble evolution in 316 steel observed in [10].

Let us recall that the theory of OR gas bubble evolution in its original form was proposed in [7] and reproduced in other studies [11,12]. A more complex description was developed later [13,14], where it was shown that small and large bubble growth laws are different. Growing small bubbles were assumed to be mechanically equilibrium as in the original theory [7]. On the other hand, large bubbles could contain gas of the same density, therefore their growth laws had a different form [14]. However, our numerical modelling showed that the simulation results did not agree with the theoretical results [15,16]. All bubbles, small and large, grow along a trajectory corresponding to the gas density [9]. Moreover, an analysis of thermodynamic system of bubbles and interstitial gas had allowed correct modification of variables in equations. Thus, a new theoretical approach was developed to explain correctly the simulation and experimental results [9].

This study of the OR bubble evolution uses the approach developed in the Lifshitz–Slezov–Wagner (LSW) theory [17,18]. Authors of this theory defined their solution as asymptotic. This was confirmed in our work [19] by numerical solution to a master equation taken for a model problem of vacancy clustering during annealing of quenched metal. It was shown that the cluster size distribution

function in Ni calculated for a long annealing time (10^7 s) at 550°C fully coincided with the asymptotic solution known from the LSW theory. Moreover, this theory was validated experimentally, for example, when studying second phase precipitation in binary alloys during annealing [20].

At the same time, there are investigations that express doubt regarding the asymptotic form of solution in the LSW theory. For example, another asymptotic solution of the OR cluster growth problem is given in [21]. However, this question is still debatable and requires additional examination. Therefore, according to tradition, the LSW theory solution will be hereinafter assumed as asymptotic.

This study is focused on theoretical investigation of gas bubble growth kinetics in metals and alloys filled either with monoatomic or diatomic gas. It is supposed that bubble evolution follows the OR mechanism that is responsible for accumulation of helium bubbles (monoatomic gas) and hydrogen bubbles (diatomic gas) in metal under annealing conditions. Time and temperature dependences for an average radius and total concentration of bubbles, as for helium and hydrogen, are successfully formulated using an approach proposed in [9]. The established analytical temperature dependences are compared with the results of a number of experimental studies.

Comparative analysis is conducted using the experimental data concerning helium bubble growth in four materials: nickel, austenitic stainless steel, copper and tungsten. The reasons for choosing these materials are as follows. Nickel is a well studied model material included in austenitic stainless steels. 316L austenitic stainless steel is used as a structural material in light water reactors and fast breeder reactors. It is also known that 316L(N) steel was chosen as a main structural material for the ITER nuclear fusion reactor project. A large amount of experimental data, including from modern studies, is also available. Tungsten is one of the candidates for producing first wall shield block components (tiles) [22]. Being a material with high thermal conductivity, copper is included in first wall bonding elements between a tile and the first wall made of heat-resistant chrome zirconium copper.

This study focuses on the theoretical analysis and comparison between the analytical and experimental data. Model assumption needed for theoretical description of gas bubble growth during annealing are described in Section 2. The general asymptotic description of n -atomic gas bubble evolution in metals and alloys is given in Section 3. Theoretical temperature dependences of monoatomic gas (helium) bubble growth are compared with the experimental measurements of the observed variables in Section 4. The main conclusions of the study are formulated in Section 5.

2. Model assumption

We use the asymptotic approach of the LSW theory proposed for describing the OR growth of single-component

clusters. When using this approach to obtain a solution of a more complex problem: gas-vacancy clusters (bubbles) in metals during annealing, the following models assumptions will be used: (1) the number of gas atoms implanted in metal remains finite and unchanged during annealing; (2) the number of thermal vacancies is unlimited; (3) the concentration of vacancies is in thermal equilibrium and is considered to be constant; (4) all bubbles are treated as immobile defects; (5) the fraction of gas atoms accumulated in the lattice is much lower compared with that inside bubbles; (6) dissociative (interstitial) mechanism of gas atom migration between bubbles in the lattice is the preferable one.

The growing gas-vacancy clusters are also considered to form a sufficiently rarefied bubble population in the lattice. Therefore, the effects associated with mutual bubble overlapping will be considered as insignificant and not affecting the bubble size distribution function.

Experimentally observed bubble sizes (> 2 nm) are used to estimate gas pressure in bubbles as sufficiently high (~ 10 GPa). Therefore, for bubble coalescence analysis, approximation with equation of real gas state will be used.

Moreover, it is assumed that polyatomic gas (e.g. hydrogen) molecules interacting with lattice atoms during redissolution are dissociated immediately. This is possible on the assumption that surface atoms fail to form strong chemical bonds with gas atoms. Therefore, hydrogen atom accumulation on the surface of bubbles, i.e. adsorption and chemisorption, will be neglected.

3. Theory of Ostwald gas bubble coalescence

According to the above-mentioned model assumptions, general analysis of OR bubble coalescence is carried out. The study is performed to obtain time and temperature dependences of gas bubble evolution.

3.1. Kinetics equation

Evolution of gas-vacancy clusters interacting with point defects (PD), i.e. vacancies and gas atoms, is usually studied by taking a solution to the „Master equation“ numerically in discrete two-dimensional space of dimensions n, m with the step equal to unity.

$$\frac{df(n, m, t)}{dt} = (J_n(n-1, m, t) - J_n(n, m, t)) + (J_m(n, m-1, t) - J_m(n, m, t)), \quad (1)$$

where n and m are the numbers of vacancies and gas atoms in the cluster, respectively. Equation (1) uses $f(n, m, t)$ and $J_n(n, m, t)$, $J_m(n, m, t)$ is the function of cluster size distribution and cluster fluxes in directions n and m of the two-dimensional space, respectively. These fluxes are

defined by cluster-PD interaction rates:

$$J_n(n, m, t) = P_v(n, t)f(n, m, t) - Q_v(n+1, m, t)f(n+1, m, t),$$

$$J_m(n, m, t) = P_g(n, t)f(n, m, t) - Q_g(n, m+1, t)f(n, m+1, t),$$

where $P_v(n, t)$, $Q_v(n, m, t)$, $P_g(n, t)$ and $Q_g(n, m, t)$ are reaction rates of mobile PD capture (P) and evaporation (Q) clusters giving rise to the change of cluster sizes n and m , respectively.

Equation (1) is also identical to the Zeldovich equation proposed in [23] extended for the dual vacancy and gas atom solution case. Results of computational simulation using this equation are shown, for example, in [8,9].

To solve cluster evolution problems by analytical methods, the equivalent Fokker–Planck (FP) equation, derived from transformation of equation (1), is used. Proceeding to the derivatives in the continuous space of dimensions x, y on the right-hand side of the equation, it is easy to derive the FP equation as:

$$\begin{aligned} \frac{\partial f(x, y, t)}{\partial t} = & -\frac{\partial}{\partial x} \left(V_x f + \frac{\partial}{\partial x} (D_x f) \right) \\ & - \frac{\partial}{\partial y} \left(V_y f + \frac{\partial}{\partial y} (D_y f) \right). \end{aligned} \quad (2)$$

In this equation, the rates characterizing the ordered cluster motion in the size space, as shown in [24], are equal

$$\left\{ \begin{array}{l} V_x = [P_v(x) - Q_v(x, y)] \\ V_y = [P_g(x) - Q_g(x, y)] \end{array} \right\}. \quad (3)$$

On the other hand, diffusion terms according to [25], are written as:

$$\left\{ \begin{array}{l} D_x = \frac{1}{2} [P_v(x) + Q_v(x, y)] \\ D_y = \frac{1}{2} [P_g(x) + Q_g(x, y)] \end{array} \right\}. \quad (4)$$

Coefficients given in equation (4) describe nucleation of a new phase and growth of nuclei from the very supersaturated PD solution. At the next stage, clusters of a new phase become sufficiently large and gas atom concentration is getting low. Then, the evolution of gas-vacancy clusters may proceed according to the OR mechanism. In this case, large clusters grow due to absorption of smaller ones.

3.2. Gas-vacancy cluster evolution

At the stage of gas-vacancy cluster evolution according to the OR mechanism, cluster growth at the expense of fluctuation is impossible. By excluding the diffusion components, equation (2) is transformed to a hydrodynamic equation:

$$\frac{\partial f(x, y, t)}{\partial t} = -\frac{\partial}{\partial x} (V_x f) - \frac{\partial}{\partial y} (V_y f). \quad (5)$$

The asymptotic cluster evolution problem will be solved in an infinite time interval t and in an unlimited size space x, y . In the initial time $t = 0$, cluster size distribution may be various, since the solution of equation (5) is a universal distribution function, which independent of the initial cluster distribution.

To solve equation (5), it is necessary to determine V_x and V_y . Kinetics equations (3) describe the cluster growth that might be treated as a motion in the field of force F in some range of dimensions x, y :

$$F = -\left(\frac{\partial \Phi(x, y)}{\partial x} + \frac{\partial \Phi(x, y)}{\partial y} \right), \quad (6)$$

where $\Phi(x, y)$ is the thermodynamic potential. This potential modifies gas-vacancy clusters passing through a sequence of equilibrium states from a „monomer“ to a bubble with sizes x, y with an equilibrium concentration:

$$N(x, y) = N_0 \exp \left[-\frac{\Phi(x, y)}{k_B T} \right]. \quad (7)$$

Using equations (6) and (7), it can be shown that thermodynamic forces expressed through the logarithms of equilibrium concentration ratio between the clusters with neighboring sizes $N(x, y)$, $N(x', y)$ and $N(x, y')$ are equal

$$\begin{aligned} \frac{\partial \Phi(x, y)}{\partial x} &= k_B T \ln \left(\frac{N(x', y)}{N(x, y)} \right), \\ \frac{\partial \Phi(x, y)}{\partial y} &= k_B T \ln \left(\frac{N(x, y')}{N(x, y)} \right), \end{aligned} \quad (8)$$

where $x > x'$ and $y > y'$. Note that continuous variables x, x', y and y' , taken for $N(x, y)$ in case of discrete distribution of $N(n, m)$ shall be represented by their discrete equivalents in the size space with unit steps: $n, n-1, m$ and $m-1$, respectively.

In the thermodynamic equilibrium conditions, detailed balance is kept between the gas-vacancy clusters and point defects (vacancies and gas atoms):

$$\begin{aligned} Q_v(x, y)N(x, y) &= P_v(x')N(x', y), \\ Q_g(x, y)N(x, y) &= P_g(x)N(x, y'). \end{aligned} \quad (9)$$

Using equations (8) and (9), kinetics equations (3) for the cluster growth rate in the directions of x and y are transformed to:

$$\left\{ \begin{array}{l} \frac{dx}{dt} = -P_v(x) \left[\frac{1}{k_B T} \left(\frac{\partial \Phi(x, y)}{\partial x} \right) \right] \\ \frac{dy}{dt} = \frac{1}{\xi} P_g(x) \left\{ 1 - \exp \left[\frac{1}{k_B T} \left(\frac{\partial \Phi(x, y)}{\partial y} \right) \right] \right\} \end{array} \right\}, \quad (10)$$

where $P_v(x) = 3\beta^2 x^{1/3} D_v c_v$ and $P_g(x) = 3\beta^2 x^{1/3} D_g c_g$ are the vacancy and gas atom absorption rates, respectively, c_v and c_g are atomic concentrations of vacancies and gas in the lattice, respectively; $\beta = (4\pi/3\Omega)^{1/3}$ is the geometrical factor, Ω is the atomic volume; ξ is the dimensionless

numerical variable, which is equal to 1 for monoatomic gas and to 2 for diatomic gas.

In equation (10), the rate dx/dt is linearized assuming that $P_v(x) \approx P_v(x')$, if gas-vacancy clusters are large enough. The rate dy/dt is represented by taken into account that diatomic gas ($\xi = 2$) undergoes dissociation before the gas atoms leave a surface of the cluster into the metal lattice.

3.3. Thermodynamic system properties

We determine the thermodynamic potential of the system of PD and gas-vacancy clusters as a sum:

$$\Phi(x, y) = -x\mu_v + E(x) - \xi y\mu_g + F(x, y), \quad (11)$$

where $\mu_v = k_B T \ln(c_v/c_{v0})$ and $\mu_g = k_B T \ln(c_g) + \Psi(T)$ are the chemical potentials of vacancies and gas atoms in the lattice, here, $\Psi(T)$ is the temperature-dependent function of gas atoms dissolved in metal; c_{v0} is the equilibrium concentration of vacancies; $E(x)$ is the free energy of gas-vacancy cluster surface consisting of x vacancies equal to $3\gamma\beta\Omega x^{2/3}$, γ is the cluster surface energy; $F(x, y)$ is the free energy of monoatomic and diatomic gas molecules inside the cluster.

Expression describing the free energy of non-ideal gas $F(x, y)$ was proposed in [26]:

$$F(x, y) = y k_B T \left\{ \ln \left[e^{-1} \frac{y}{x} Z(x/y, T) \right] + \frac{f(T)}{k_B T} \right\}. \quad (12)$$

where $f(T)$ is the temperature-dependent function of gas atoms in bubbles.

The equation of state for real gases in approximation of the reduced Van der Waals equation [27] can be written as:

$$\frac{p(x, y, T)}{k_B T} = \frac{1}{\Omega} \frac{y}{x} \left[1 / \left(1 - B_2(T) \frac{1}{\Omega} \frac{y}{x} \right) \right], \quad (13)$$

where the bracket expression — is the gas compressibility factor $Z(y/x, T)$ that is > 1 for non-ideal gases, $B_2(T)$ is the second virial coefficient that takes into account the most probable pairwise collisions of gas atoms whose size is equal to the helium atom volume $\sim 10^{-30} \text{ m}^3$.

Differentiating the left-hand and right-hand sides of equation (11) taking into account equations (12), (13), we obtain the expressions for thermodynamic forces written as:

$$\left\{ \begin{array}{l} \frac{\partial \Phi(x, y)}{\partial x} = -k_B T \ln \left(\frac{c_v}{c_{v0}} \right) + \frac{2\gamma\Omega}{R(x)} - p(x, y, T)\Omega, \\ \frac{\partial \Phi(x, y)}{\partial y} = -\xi k_B T \ln(c_g) - \xi \Psi(T) + k_B T \\ \quad \times \ln \left(\frac{p(x, y, T)\Omega}{k_B T} \right) + f(T) + p(x, y, T)B_2(T) \end{array} \right\}, \quad (14)$$

where $R(x)$ is the cluster radius consisting of x vacancies. In accordance with our model assumptions, vacancy concentration is $c_v = c_{v0}$, therefore the logarithmic term in the first equation may be neglected.

3.4. Law of gas dissolution in metal

After substitution of equation (14) into equation (10), expressions for cluster dimension variation rates are obtained:

$$\left\{ \begin{array}{l} \frac{dx}{dt} = -3\beta^3 R(x) D_v c_{v0} \left[\frac{1}{k_B T} \left(\frac{2\gamma\Omega}{R(x)} - p(x, y, T)\Omega \right) \right] \\ \frac{dy}{dt} = \frac{1}{\xi} 3\beta^3 R(x) D_g c_g \left(1 - \frac{K^\xi}{c_g^\xi} p(x, y, T)\Omega \right) \end{array} \right\}, \quad (15)$$

where K is the temperature-/pressure-dependent gas solubility factor that is written as:

$$K^\xi = \frac{1}{k_B T} \exp \left(-\frac{\xi \psi(T, p)}{k_B T} \right), \quad (16)$$

where the energy of gas atom re-dissolution from bubbles to the metal lattice is equal to

$$\psi(T) = \Psi(T) - \frac{1}{\xi} [f(T) + p(T)B_2(T)].$$

Assuming that $dy/dt = 0$ in equation (15), a generalized expression of the Henry's law ($\xi = 1$) and Sieverts's law ($\xi = 2$) is derived:

$$c_g = K(p(T)\Omega)^{1/\xi}. \quad (17)$$

Expression (17) follows from the equilibrium thermodynamic condition between gas accumulated in bubbles and diluted solution of gas atoms in the lattice.

3.5. Trajectories of bubble growth and critical radius

Using the bubble equilibrium condition, setting the right-hand side of equations (15) to zero, two expressions for the bubble radius are derived depending on the number of gas atoms accumulated in the bubble:

$$\begin{aligned} R &= \left[y \frac{1}{\beta^3 R} \left(\frac{k_B T}{2\gamma\Omega/R} + \frac{B_2}{\Omega} \right) \right]^{1/2}, \\ R &= \left[y \frac{1}{\beta^3} \left(\left(\frac{c_g^*}{c_g} \right)^\xi + \frac{B_2}{\Omega} \right) \right]^{1/3}, \end{aligned} \quad (18)$$

where $c_g^* = \exp[-\psi/k_B T]$ is the concentration of dissolved gas atoms in the lattice that are in thermodynamic equilibrium with bubbles.

The first expression in equation (18) determines the growth path of mechanically equilibrium bubbles when the gas pressure is balanced by the Laplace pressure ($p = 2\gamma/R$). The second expression determines bubble growth under conditions of chemical equilibrium between gas atoms accumulated in the bubbles and atoms in the lattice ($\mu_R = \xi\mu_g$, where μ_R is the chemical potential of gas atoms in the bubble). The latter means that, as it follows from equation (18), the growing bubbles contain gas with the same density ($y/x = \text{const}$). According to the results of

our computational simulation [9], bubble growth by the OR mechanism develops along the trajectory of the chemical equilibrium. Conversely, in case of the BMC mechanism, according to the results of computations given in [8], bubbles grow along the trajectory of mechanical equilibrium.

Using equations (18), we find the point of intersection of these trajectories. It corresponds to the critical bubble radius R_0 and the number of gas atoms/molecules y_0 inside:

$$R_0 = \left(\frac{K}{c_g}\right)^\xi 2\gamma\Omega = \left(\frac{c_g^*}{c_g}\right)^\xi R_0^* Z^*,$$

$$y_0 = \frac{4}{3}\pi R_0^3 \left(\frac{R_0^* Z^*}{R_0 Z}\right) \frac{1}{\Omega}, \quad (19)$$

where $R_0^* = 2\gamma(\Omega - B_2)/k_B T$ is the critical bubble radius; $Z^* = Z(\rho_g^*, T)$ is the compressibility factor when the density of gas atoms in the bubble is $\rho_g^* = 1$. This corresponds to the case when the number of gas atoms and vacancies in the bubble are equal ($x_0 = y_0$).

Thus, supersaturation c_g/c_g^* has a corresponding critical radius R_0 , when gas in the mechanically equilibrium bubble is simultaneously in equilibrium with the gas solution.

3.6. Explanation of bubble evolution mechanism

In accordance with equation (18), the radius of growing bubbles R is unambiguously defined by the number of accumulated gas atoms y . This makes it possible to simplify a description of the process by rearranging the equations written for x and y to the single-variable equation depending on R .

First, we put equation (14) in the generalized form:

$$\left\{ \begin{array}{l} \frac{\partial \Phi}{\partial x} = (p_R - p_0)\Omega \\ \frac{\partial \Phi}{\partial y} = \mu_R - \xi \mu_g = k_B T \ln\left(\frac{p_R}{p_0}\right) + (p_R - p_0)B_2 \\ \approx (p_R - p_0)\Omega \left(\left(\frac{c_g^*}{c_g}\right)^\xi + \frac{B_2}{\Omega} \right) \end{array} \right\}, \quad (20)$$

where $p_R = 2\gamma/R(x)$ is the pressure of a growing gas bubble with R ; p_0 is the gas pressure within a bubble with R_0 ;

$$\mu_R = k_B T \ln(p_R \Omega / k_B T) + f(T) + p_R B_2(T)$$

is the chemical potential of gas atoms in the bubble. In equation (20), the pressure ratio is slightly different from unity ($0 < (p_R/p_0) < 2$). By expanding the logarithmic function in a series, the right-hand side of the equation may be approximated by a linear function.

Now, using the bubble growth path expression from equation (18) for the case when $\rho_g = \text{const}$, equation (20) is written as:

$$\left\{ \begin{array}{l} \left(-\frac{\partial \Phi}{\partial x}\right) \frac{1}{\Omega} = p_0 - p_R \\ \rho_g \left(-\frac{\partial \Phi}{\partial y}\right) \frac{1}{\Omega} \approx p_0 - p_R \end{array} \right\}. \quad (21)$$

It can be seen that these equations coincide, if $dy = \rho_g dx$. Then, taking into account the spherical shape of the bubbles: $dx = 3\beta^3 R^2 dR$, and that p_R and p_0 are equal to $2\gamma/R$ and $2\gamma/R_0$, respectively, a single equation is derived, connecting the thermodynamic force with the different gas pressures in bubbles:

$$\frac{1}{4\pi R^2} \left(-\frac{d\Phi}{dR}\right) = 2\gamma \left(\frac{1}{R_0} - \frac{1}{R}\right). \quad (22)$$

This equation provides a simple physical interpretation of gas bubble coalescence governed by the OR mechanism.

System free energy Φ changes as function of R . The maximum of free energy is in the point R_0 . It is estimated as one third of the surface energy of the bubble having critical radius.

It can be seen from equation (22), the sign of the right-hand side of this equation is always opposite to that of $\partial\Phi/\partial R$. If the bubble radius is larger than the critical one ($R > R_0$), the right-hand side of the equation is positive, then the derivative $\partial\Phi/\partial R$ shall be negative. Thus, bubbles grow infinitely by capturing gas atoms and the corresponding number of vacancies. On the contrary, when ($R < R_0$), the right-hand side of the equation becomes negative, then $\partial\Phi/\partial R$ takes positive indication. In this case, bubbles only get smaller by evaporating gas together with vacancies.

3.7. Bubble growth rate

Equation (22) depending on one variable — R , makes it possible to modify equation (5) by transforming to the continuity equation written as:

$$\frac{\partial f(R, t)}{\partial t} = -\frac{\partial}{\partial R} [V_x(R, t) + V_y(R, t)]f(R, t). \quad (23)$$

Assuming that the forces $\partial\Phi/\partial x$ and $\partial\Phi/\partial y$ are linearly associated with the velocities dx/dt and dy/dt , then by substituting the corresponding expressions from (20), the following set of equations is derived

$$\left\{ \begin{array}{l} \frac{dx}{dt} = 3\beta^3 R(x) D_v c_{v0} \left[(p_0 - p_R) \frac{\Omega}{k_B T} \right] \\ \frac{dy}{dt} = \frac{1}{\xi} 3\beta^3 R(x) D_g c_g \left(1 - \frac{K^\xi}{c_g^\xi} p_R \Omega \right) Z(y/x, T) \end{array} \right\}. \quad (24)$$

Here, the expression for dy/dt differs from equation (15) in term Z . Therefore, for small bubbles, the gas may be explicitly considered as nonideal, $Z > 1$. Alternately, it is ideal in large bubbles, $Z = 1$, then both sets of equations (24) and (15) correspond.

By transforming and summing velocities dx/dt and dy/dt from equation (24), one obtains bubble radius variation with

time:

$$V(R, t) = \frac{1}{R} \left(D_v c_{v0} + \frac{1}{\xi} \left(\frac{1}{\rho_g} \right)^{2-1/\xi} Z^{1/\xi} D_g c_g^* \right) \times \left[\left(\frac{c_g}{c_g^*} \right)^\xi - \frac{2\gamma\Omega}{Rk_B T} \right]. \quad (25)$$

Expression of this rate is similar to that obtained in [17]. Bubble growth rate is determined by the sum of volume diffusion of vacancies and gas atoms in the lattice. c_g/c_g^* serves as supersaturation, instead of $(c-c_\infty)/c_\infty$ supersaturation with „dissolved atoms of substance“ in the LSW theory.

The rate $V(R, t)$ is applied to find asymptotic solutions of equation (23), by using a technique proposed in [12]. Dependences of gas bubble evolution in time are also established.

3.8. Two asymptotic cases

According to equation (25), two asymptotic cases are distinguished: $\rho_g = 1$ and $\rho_g \ll 1$, which characterize the earlier and later bubble coalescence stages, respectively.

Let us consider a new function $f(R, \tau)$ defined with respect to a new time τ :

$$\frac{\partial f(R, \tau)}{\partial \tau} = -\frac{\partial}{\partial R} (V(R, \tau) f(R, \tau)), \quad (26)$$

where $V(R, \tau)$ is the rate of bubble radius variation written in a new time scale.

When the gas density $\rho_g = 1$ and the critical bubble radius is equal to R_0^* , this corresponds to the growing stage of smaller bubble size ($R_0 \approx 2$ nm). It can be shown that the rate given in equation (25) is written as:

$$V(R, t) = \frac{1}{R} (D_v^{\text{eff}}(c_{v0} + c_g^*)) \left[\left(\frac{c_g}{c_g^*} \right)^\xi - \frac{2\gamma\Omega}{Rk_B T} \right], \quad (27)$$

where

$$D_v^{\text{eff}} = (D_v c_{v0} + (1/\xi)(Z^*)^{1/\xi} D_g c_g^*) / (c_{v0} + c_g^*)$$

is the effective diffusion coefficient. Assuming that $c_{v0} \gg c_g^*$ and defining the new time scale variable

$$\tau = \frac{3}{2} \left(\frac{2\gamma\Omega}{k_B T} \right) (D_v^{\text{eff}} c_{v0}) t, \quad (28)$$

then equation (27) is written as

$$V(R, \tau) = \frac{2/3}{R} \left(\frac{1}{R_0(\tau)} - \frac{1}{R} \right). \quad (29)$$

Otherwise, when the gas density in bubbles decreases considerably ($\rho_g \ll 1$), critical radius R_0 increases and becomes much higher than R_0^* . Then, considering that

$Z = 1$, expression for the growth rate from equation (25) is written in a general form for an arbitrary value of ξ :

$$V(R, t) = \frac{1}{R} \left(\frac{1}{\xi} \left(\frac{1}{\rho_g} \right)^{2-1/\xi} D_g c_g^* \right) \left[\left(\frac{c_g}{c_g^*} \right)^\xi - \frac{2\gamma\Omega}{Rk_B T} \right]. \quad (30)$$

And choosing a new time

$$\tau = \frac{1}{\xi} \left[\left(\frac{3\xi}{\xi+1} \right) \left(\frac{3}{2} \right)^{1-1/\xi} \right]^{-1} \left(\frac{k_B T}{2\gamma\Omega} \right)^{1-1/\xi} (D_g c_g^*) t, \quad (31)$$

equation (30) is rearranged to

$$V(R, \tau) = \frac{1}{R} \left[\left(\frac{3\xi}{\xi+1} \right) \left(\frac{3}{2} R_0(\tau) \right)^{1-1/\xi} \right] \left(1 - \frac{R_0(\tau)}{R} \right). \quad (32)$$

By defining the bubble growth rates for two asymptotic cases, let us find asymptotic solution $f(R, \tau)$.

3.9. Properties of asymptotic solution

Asymptotic solution to equation (26) can be obtained as a product of two terms. One of these terms depends on time, and the second one is the function of time-independent variable

$$f(R, \tau) = \tau^a g(R\tau^b), \quad (33)$$

where a and b are the constants of time that has to be defined. To define these constants, we use the algebraic moment formulation for the function $f(R, \tau)$ by defining the i -th moment as

$$\mu_i = \int_0^\infty R^i f(R, \tau) dR. \quad (34)$$

By using this definition for the algebraic moments, conservation law of gas in the lattice is written as:

$$M = \xi \rho_g \beta^3 \mu_3 + c_g \equiv \text{const}, \quad (35)$$

where M is the total number of implanted gas atoms in the lattice, μ_3 is the third moment of the bubble distribution function, physical meaning of which is the bubble volume fraction. In case of the asymptotic solution, μ_3 slightly depends on time. It is assumed, that μ_3 increases slowly as bubbles grow with simultaneous decreasing of gas density ρ_g in bubbles.

Introducing the new function $g(u)$ depending on $u = R\tau^b$, one defines the i -th moment:

$$\alpha_i = \int_0^\infty u^i g(u) du. \quad (36)$$

Combining equations (33), (34) and (36), we find

$$\mu_i = \tau^{a-b(i+1)} \alpha_i. \quad (37)$$

Where α_i is the term being independent on time τ . Using also the assumption that μ_3 is of time independence, from equation (37), the relation for the constants is as follows:

$$a = 4b.$$

In case of the smaller bubbles ($R_0 = R_0^*$), the following recurrent relation is found for $d\mu_i/d\tau$:

$$\frac{d\mu_i}{d\tau} = i \frac{2}{3} \left(\frac{1}{R_0} \mu_{i-2} - \mu_{i-3} \right), \tag{38}$$

For the larger bubbles ($R_0 \gg R_0^*$), such the relation is written as:

$$\frac{d\mu_i}{d\tau} = i \left(\frac{3\xi}{\xi + 1} \right) \left(\frac{3}{2} \right)^{1-1/\xi} \left(R_0^{1-1/\xi} \mu_{i-2} - R_0^{2-1/\xi} \mu_{i-3} \right). \tag{39}$$

Let us apply the condition $d\mu_3/d\tau = 0$ to solve equations (38), (39). In both cases, bubble radius R_0 has the identical time dependence:

$$R_0 = \left(\frac{\alpha_1}{\alpha_0} \right) \tau^{-b}. \tag{40}$$

If using equation (40), by excluding μ_i and substituting equation (37) into equations (38), (39), we have

$$b = \left\{ \begin{array}{ll} -\frac{1}{3}, & R_0 = R_0^* \\ -\frac{\xi}{\xi + 1}, & R_0 \gg R_0^* \end{array} \right\}, \tag{41}$$

The required constants a and b are defined, now equation (26) can be solved.

3.10. Universal distribution function

In case of the smaller bubbles $R_0=R_0^*$, let us substitute the solution $f(R, \tau)=\tau^{-4/3}g(R\tau^{-1/3})$ together with the growth rate $V(R, \tau)$ taken from equation (29) into (26). Moving on to the function $g(u)$, and taking into consideration that $u = (\alpha_1/\alpha_0)R/R_0$, we obtain

$$\frac{\partial g(u)}{\partial u} u \left(u^3 - 2 \frac{\alpha_0}{\alpha_1} u + 2 \right) + g(u) \left(4u^3 + 2 \frac{\alpha_0}{\alpha_1} u - 4 \right) = 0. \tag{42}$$

In case of the larger bubbles $R_0 \gg R_0^*$, we find the solution in the form

$$f(R, \tau) = \tau^{-4\xi/(\xi+1)} g(R\tau^{-\xi/(\xi+1)}).$$

If substituting this into equation (26), and the growth rate $V(R, \tau)$ taken from equation (32), it gives

$$\begin{aligned} & \frac{\partial g(u)}{\partial u} u \left(u^3 - \left(\frac{3}{2} \frac{\alpha_1}{\alpha_0} \right)^{1-1/\xi} \left(3u - 3 \frac{\alpha_1}{\alpha_0} \right) \right) \\ & + g(u) \left(4u^3 + \left(\frac{3}{2} \frac{\alpha_1}{\alpha_0} \right)^{1-1/\xi} \left(3u - 6 \frac{\alpha_1}{\alpha_0} \right) \right) = 0. \end{aligned} \tag{43}$$

Assuming that ratio of α_1/α_0 is equal to 2/3, equations (42), (43) appear to be identical, and the result of their integration is equivalent to the universal size distribution function known from the LSW theory:

$$g(u) = \left\{ \begin{array}{ll} e^A e^{1/3} \frac{u^2}{(2+u)^{7/3}(1-u)^{11/3}} \exp \left[\frac{-1}{(1-u)} \right], & u < 1 \\ 0, & u > 1 \end{array} \right\}, \tag{44}$$

where A is the integration constant defined by normalization of $g(u)$. Note also that equation (43) doesn't depend on the value of the parameter ξ . Thus, the asymptotic solution is independent on the number of gas atoms in a molecule.

Integration of the function $g(u)$ given in equation (44) within the range of zero and unity yields exact values:

$$\alpha_0 = e^A e^{1/3} [3e 2^{4/3}]^{-1}, \quad \alpha_1 = e^A e^{1/3} [3^2 e 2^{1/3}]^{-1}.$$

Thus, the assumption that $\alpha_1/\alpha_0 = 2/3$ is correct.

3.11. Time dependences

Metal properties are defined by the influence of microstructural elements such as gas-vacancy agglomerations, which are of great physical interest. Observed variables such as the total bubble density and mean radius may be defined as $N = \mu_0$ and $R = \mu_1/\mu_0$, respectively, using the first two initial moments. The volume fraction of bubbles $N_v = \beta^3 \mu_3$ considering that $\langle R^3 \rangle \approx \langle R \rangle^3$ can be approximately given by a combination of N and R :

$$\frac{\Delta V}{V} \equiv N_v \approx \beta^3 R^3 N. \tag{45}$$

By use of the conservation law formulated in equation (35), we obtain the general relationship between concentration and radius:

$$N = \left[\frac{(M - c_g)}{\xi \beta^3} \frac{Z}{R_0^* Z^*} \right] \frac{1}{R^2}. \tag{46}$$

Taking into consideration the features of each asymptotic case for small and larger bubbles, this expression can be written as

$$N = \left\{ \begin{array}{ll} \frac{(M - c_g)}{\xi \beta^3} \left(\frac{k_B T}{2\gamma(\Omega - B_2)} \right) \frac{1}{R^2}, & R_0 = R_0^* \\ \frac{M}{\xi \beta^3} \left(\frac{k_B T}{2\gamma\Omega} \right) \frac{1}{R^2}, & R_0 \gg R_0^* \end{array} \right\}. \tag{47}$$

In the former case, correction of the pair interaction B_2 in nonideal gas approximation is taken into account, in the latter case, gas is considered to be ideal and the interstitial gas atom concentration c_g is accepted to be negligibly low. It is worth noting that the expression for large bubbles (the second expression) is also valid for the BMC mechanism.

By using these relations established for the mean bubble radius in equation (40) and concentrations in equation (47),

Table 1. Time dependences of the mean bubble radius and total concentration for monoatomic gas (helium) and diatomic gas (hydrogen)

	ξ	$R(T, t)$	$N(M, T, t)$
$R_0 = R_0^*$	1	$\left(\frac{2\gamma(\Omega - B_2)}{k_B T}\right)^{1/3} \left[\left(\frac{2}{3}\right)^2 (D_v^{\text{eff}} c_{v0}) t\right]^{1/3}$	$(M - c_g) \frac{1}{\beta^3} \left(\frac{k_B T}{2\gamma(\Omega - B_2)}\right)^{5/3} \left[\left(\frac{2}{3}\right)^2 (D_v^{\text{eff}} c_{v0}) t\right]^{-2/3}$
	2	$\left(\frac{2\gamma(\Omega - B_2)}{k_B T}\right)^{1/3} \left[\left(\frac{2}{3}\right)^2 (D_v^{\text{eff}} c_{v0}) t\right]^{1/3}$	$\frac{(M - c_g)}{2} \frac{1}{\beta^3} \left(\frac{k_B T}{2\gamma(\Omega - B_2)}\right)^{5/3} \left[\left(\frac{2}{3}\right)^2 (D_v^{\text{eff}} c_{v0}) t\right]^{-2/3}$
$R_0 \gg R_0^*$	1	$\left[\left(\frac{2}{3}\right)^3 (D_g c_g^*) t\right]^{1/2}$	$M \frac{1}{\beta^3} \left(\frac{k_B T}{2\gamma\Omega}\right)^1 \left[\left(\frac{2}{3}\right)^3 (D_g c_g^*) t\right]^{-1}$
	2	$\left(\frac{2\gamma\Omega}{k_B T}\right)^{-1/3} \left[\left(\frac{1}{3}\right)^2 (D_g c_g^*) t\right]^{2/3}$	$\frac{M}{2} \frac{1}{\beta^3} \left(\frac{k_B T}{2\gamma\Omega}\right)^{1/3} \left[\left(\frac{1}{3}\right)^2 (D_g c_g^*) t\right]^{-4/3}$

their time dependences in both asymptotic cases can be easily derived:

$$R(t) = \left\{ \begin{array}{l} \left(\frac{2\gamma(\Omega - B_2)}{k_B T}\right)^{1/3} \left[\left(\frac{2}{3}\right)^2 (D_v^{\text{eff}} c_{v0}) t\right]^{1/3}, R_0 = R_0^* \\ \left(\frac{2\gamma\Omega}{k_B T}\right)^{-\frac{\xi-1}{\xi+1}} \left[\frac{1}{\xi} \left(\frac{\xi+1}{3\xi}\right) \left(\frac{2}{3}\right)^2 (D_g c_g^*) t\right]^{\frac{\xi}{\xi+1}}, R_0 \gg R_0^* \end{array} \right\},$$

$$N(M, t) = \left\{ \begin{array}{l} \frac{(M - c_g)}{\xi\beta^3} \left(\frac{k_B T}{2\gamma(\Omega - B_2)}\right)^{5/3} \left[\left(\frac{2}{3}\right)^2 (D_v^{\text{eff}} c_{v0}) t\right]^{-2/3}, \\ R_0 = R_0^* \\ \frac{M}{\xi\beta^3} \left(\frac{k_B T}{\gamma\Omega}\right)^{-\frac{\xi-3}{\xi+1}} \left[\frac{1}{\xi} \left(\frac{\xi+1}{3\xi}\right) \left(\frac{2}{3}\right)^2 (D_g c_g^*) t\right]^{-\frac{2\xi}{\xi+1}}, \\ R_0 \gg R_0^* \end{array} \right\}. \tag{48}$$

Let us formulate these dependences as applied to the cases when parameter ξ is equal to 1 for monoatomic gas, i.e. for helium, and to 2 for hydrogen. The results of this substitution are given in Table 1.

Note that bubble density N depends on the number of gas atoms implanted in material M , while the mean bubble radius R does not. This distinguishes the OR bubble evolution from the BMC mechanism, in which the mean radius value depends on implanted gas atoms M .

This theoretical analysis offers a new approach for studying monoatomic and diatomic gas bubble evolution proceeding by the OR mechanism. It can be validated by a comparison between the obtained theoretical results and experimental data.

4. Analysis of experimental data

By using the dependences obtained for the mean bubble radius $R(T, t)$ and the bubble density $N(M, T, t)$ in case

of monoatomic gas ($\xi = 1$) from Table 1, a comparison between these results and published data is performed. In this study, experimental data obtained from transmission electron microscopy (TEM) for nickel (Ni), austenitic stainless steel (316L), copper (Cu) and tungsten (W) is used. Temperature dependences were obtained for the above-listed metals and alloys by means of pre-implanted helium in the range of 300 and 1000 appm at room temperatures followed by annealing in the homologous temperature range of $\sim 0.5T_m$ and above.

4.1. Gas bubble evolution in nickel

Theoretical time and temperature dependences obtained for R and N are compared with experimental data for irradiated Ni [28]. Authors of the paper reported that the specimen were initially saturated homogeneously with helium to 1000 appm, and then annealed isochronously during 1 hour in the temperature range from 700°C to 900°C. They showed that the bubble growth rate at the grain surface is higher than within the grain. The mean radius and bubble density at the grain surface and inside the grain were calculated separately. Mean radius experimental data from [29] obtained in the temperature range from 800°C to 1050°C were also used for comparison.

Material parameters characteristic for Ni used for theoretical evaluation of gas bubble growth during annealing are listed in Table 2. They are followed by references to published sources.

Figure 1 shows the experimentally measured data for mean radius and bubble density in Ni observed close to the surface of grain boundary after annealing for about 1 hour. The authors of the experimental study assumed that the surface provides a sufficient vacancy flux for the relaxation of the initial high gas density in small bubbles ($R < 1$ nm). An unlimited source of vacancies provides bubble growth by the OR mechanism.

Figure 1, *a* shows theoretical curves that express temperature dependences defining two asymptotic solutions. The solid line corresponding to small bubble sizes locates in the lower annealing temperature range. The dashed line reflects

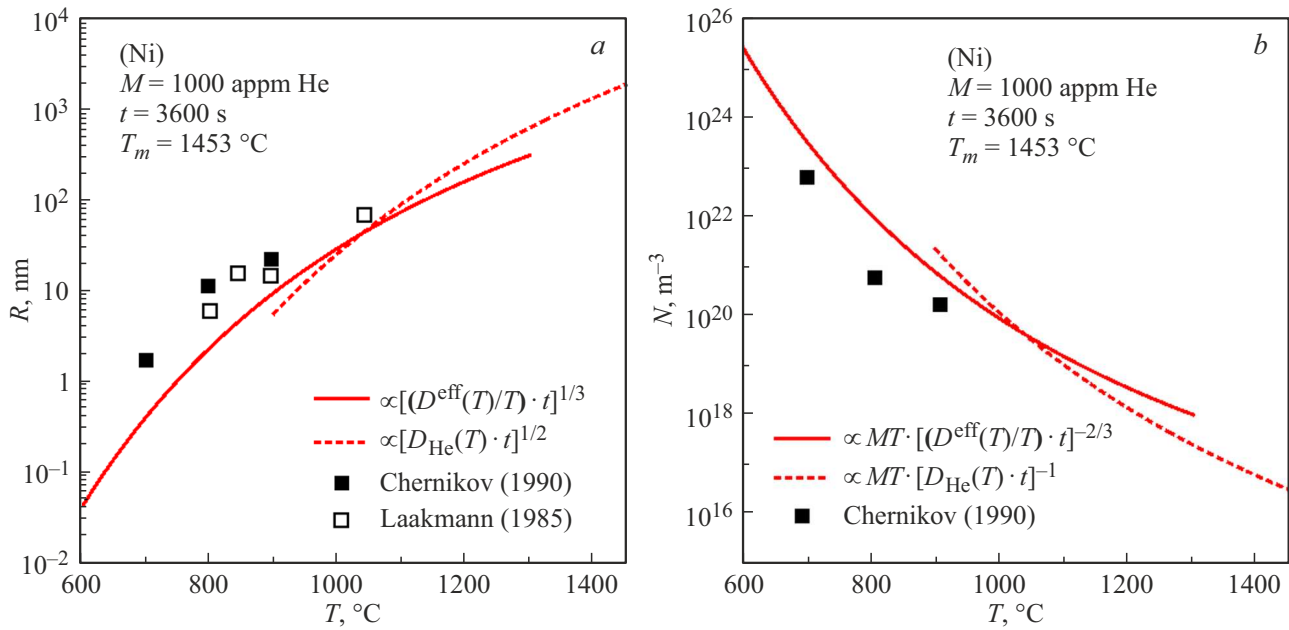


Figure 1. Comparison of the experimental measurements in nickel (black squares indicate data from [28], open squares indicate data from [29]) with temperature dependences for R (a) and for N (b) according to the OR model.

Table 2. Material properties for Ni

Property	Value	Source
Amount of implanted helium atoms M , appm	1000	[28]
Lattice constant a , Å	3.52	[30]
Atomic volume Ω , m^3	$1.094 \cdot 10^{-29}$	[31]
Vacancy formation (pre-exponential factor) C_{v0}	4.48	[31]
Vacancy formation energy E_v^f , eV	1.39	[31,32]
Vacancy diffusion (pre-exponential factor) D_{v0} , m^2/s	$9.2 \cdot 10^{-5}$	[33]
Vacancy migration energy E_v^m , eV	1.38	[31,32]
Helium diffusion (pre-exponential factor) D_{g0} , m^2/s	$6.31 \cdot 10^{-7}$	[34]
Helium migration energy E_g^m , eV	0.08	[31,35]
Surface energy γ , J/m^2	2.00	[36]
Helium dissociation energy ψ , eV	2.4	[34]

large bubble growth in the higher temperature range. At the beginning of the process, small bubbles grow due to mixed vacancies and helium atoms volume migration. At later stages, larger bubbles growth is only defined by the helium atom transfer in the lattice.

Intersection of the solid and dashed line in the point ~ 1050 °C determines the theoretical measure of the transition radius R_{tr} from conditionally small to larger bubbles. R_{tr} is sensitive to the dissociation energy ψ . Assuming that $\psi = 2.3$ eV (lower by 0.1 eV that the predicted value in [34]), then, as shown in figure 1, a, $R_{tr}(T) \approx 40$ nm.

Figure 1, b shows both theoretical curves obtained from the analysis of two asymptotic solutions. The bubble density N , as is shown in this figure, decreases predictably as the annealing temperature increases. This figure shows also intersection of the curves and transition point (~ 1050 °C) reflecting the transition from the small bubbles to the larger ones, in which growth diffusion mechanisms are different.

Figure 1, a shows that the experimental data from [28,29] agree well with the theoretically estimated $R \propto [(D^{\text{eff}}(T)/T)t]^{1/3}$, primarily in the temperature range of 900 – 1050 °C, when $R > 10$ nm. In case of lower

Table 3. Material parameters for austenitic stainless steel

Parameter	Value	Reference
Amount of implanted helium atoms M , appm	1000	[37]
Lattice constant a , Å	3.58	[38]
Atomic volume Ω , m ³	$11.47 \cdot 10^{-30}$	[39]
Vacancy formation (pre-exponential factor) C_{v0}	1.00	–
Vacancy formation energy E_v^f , eV	1.6	[40]
Vacancy diffusion (pre-exponential factor) D_{v0} , m ² /s	$6.0 \cdot 10^{-5}$	[41]
Vacancy migration energy E_v^m , eV	1.2	[41]
Helium diffusion (pre-exponential factor) D_{g0} , m ² /s	$6.31 \cdot 10^{-7}$	[34]
Helium migration energy E_g^m , eV	0.08	[42]
Surface energy γ , J/m ²	2.00	[36]
Helium dissociation energy ψ , eV	2.4	[34]

temperatures (700–800 °C), when $R < 10$ nm, a gap between theoretical and experimental curves can be seen. The most probable cause of this is the limitation of bubble size observed by the TEM methods. Large amount of small bubbles is ignored in the measurements, therefore the observed bubble size is overestimated.

Figure 1, *b* shows theoretically estimated dependence $N \propto MT[(D^{\text{eff}}(T)/T)t]^{-2/3}$ that in general reproduces the slope correctly corresponding to the experimental data from [28]. Overestimation of the expected bubble density is observed compared with the experimental data. This is probably caused by the error of experimental measurements or by the uncertainty of material parameters used in estimations.

4.2. Gas bubble evolution in 316 steel

Theoretical time and temperature dependences of R and N obtained in this work are compared with the annealing data for 316 steel from [37]. The authors reported that experimental sample of austenitic stainless steel was homogeneously implanted with 1000 appm He at 300 °C, then it was annealed in the temperature range from 650 to 1050 °C for 1 hour. It was shown that, unlike the experimental data in Ni, bubble distribution at the grain boundary and in the grain interior are the same in the examined temperature range.

Material parameters for austenitic stainless steel 316 shown in Table 3 were used in theoretical evaluation of growing bubbles in the steel during annealing. Note that PD diffusivities in austenitic stainless steel are similar to those for Ni.

Figure 2 shows the experimental measurements of the mean radius and bubble density obtained in the grain interior after annealing for 1 hour [37]. The authors found that bubble size and density after annealing appeared to

be similar both at the grain boundary and in the grain interior. They assumed that bubble growth followed the OR mechanism.

Melting temperature (T_m) for the austenitic steel is lower than that for Ni by ~ 60 °C. Intersection in the lines of temperature dependences is also shifted towards lower temperatures. Admitting $\psi = 2.4$ eV, it can be seen that this point corresponds to ~ 1010 °C, therefore, the transition radius for growing bubbles is $R_{tr} \approx 20$ nm.

Figure 2, *a* shows both temperature curves for the mean bubble radius. Small bubble growth curve (< 20 nm) (solid line) is in the lower temperature range (< 1010 °C), and large bubbles (> 20 nm) (dashed line) refer to the higher temperature region (> 1010 °C).

Theoretical dependences of bubble density evolution with temperature growth are shown in Figure 2, *b*. It can be seen also that bubble density curves are intersected in the point (~ 1010 °C). This intersection characterizes the theoretical measure between relatively small and large bubbles growing with a different rate.

The experimental data of [37], as shown in Figure 2, are generally in good agreement with theoretical dependences $R \propto [(D^{\text{eff}}(T)/T)t]^{1/3}$ and $N \propto MT[(D^{\text{eff}}(T)/T)t]^{-2/3}$ in the temperature range < 1010 °C. However, at the temperature 650 °C, when $R < 1$ nm, a noticeable discrepancy between the theory and experiment is observed. The reason for this discrepancy is probably the same as in the case of Ni, i.e. because of TEM limitations. The authors of the work [37] also noticed that a significant amount of bubbles were below actual resolution of TEM (< 2 nm) at the temperature 650 °C.

Bubble growth in 316 austenitic steel was observed by the researchers in the temperature range of 650–1050 °C, which corresponds to that for Ni. However, unlike the case for Ni, the experimental data obtained in austenitic

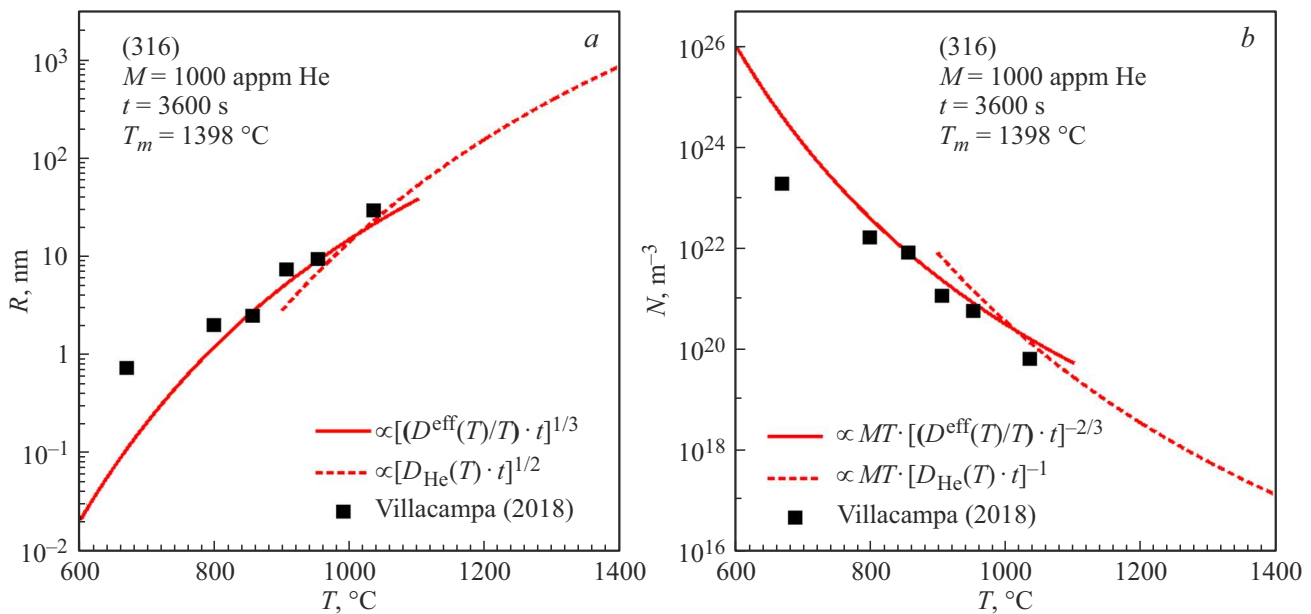


Figure 2. Comparison of the experimental measurements in 316 steel (black squares indicate data from [37]) with the temperature dependences for R (a) and for N (b) according to the OR model.

steel allow a comparison with theoretical estimates of $R \propto [D_{\text{He}}(T)t]^{1/2}$ and $N \propto MT[D_{\text{He}}(T)t]^{-1}$ which characterize the evolution of large bubbles. In Figure 2 it is evident that the experimental data taken at the temperature 1050 °C are in consistent with the theory.

Thus, the plotted theoretical dependences reproduce the experimental observations well both for small and larger bubbles. Therefore, bubble growth in 316 austenitic steel is most likely due to the OR mechanism.

4.3. Gas bubble evolution in copper

The established time and temperature theoretical dependences for R and N are compared with the data from [43] on annealing Cu specimen implanted with helium. Specimen homogeneously implanted with helium (300 appm) at 50 °C were annealed in the temperature range from 650 °C to 920 °C during 30 minutes. It was found that the bubble size in the grain boundary region appeared to be much larger than in the grain interior. A conclusion was made that, near an intensive thermal vacancy source such as grain surfaces, bubble growth follows the OR mechanism. On the other hand, dislocations within the grain do not form vacancy flux to be enough for bubble evolution governed by the OR coarsening mechanism.

Diffusion characteristics of point defects in Cu shown in Table 4 are used for theoretical estimation of bubble evolution. Data concerning the helium atom dissociation energy ψ from bubbles into the lattice is not available in the literature. Presumably the most suitable value: 1.5 eV is used for theoretical evaluations.

Figure 3 shows the experimental data for the mean radius and concentration of bubbles near the grain boundaries in

Cu. The data denoted by symbols in the figure represent our averaging of a group of experimental results obtained in [43] for each temperature.

Figure 3 also shows theoretical dependences determined on the basis of the review of asymptotic solutions of small and large bubble evolution. The point of intersection between curves of temperature dependences (solid and dashed lines) corresponds to ~ 810 °C. Assuming that $\psi = 1.5$ eV, then transition radius $R_{tr} \approx 50$ nm.

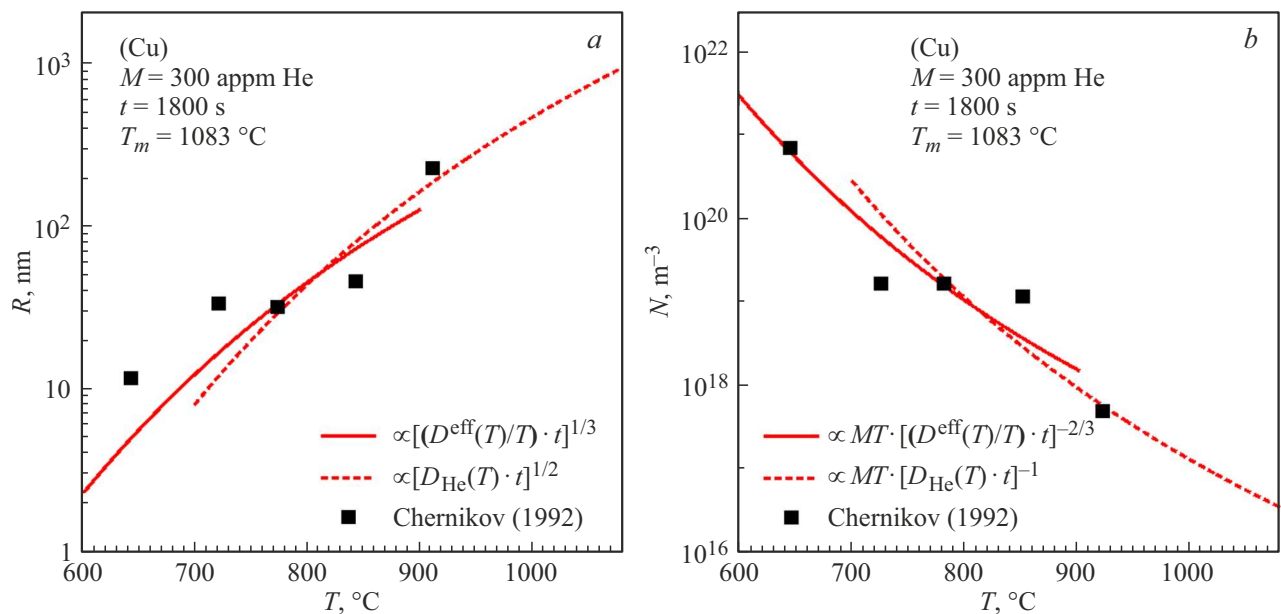
Solid lines of dependences R and N describe evolution of small bubbles (< 50 nm) related to the lower temperature range (< 810 °C). Dashed lines reflect the large bubble growth (> 50 nm) in the high temperature range (> 810 °C).

Experimentally observable bubbles presented in Figure 3 are large enough, their radius is > 10 nm in the range from 650 to 920 °C. Theoretical dependence of the mean radius $R \propto [(D^{\text{eff}}(T)/T)t]^{1/3}$ adequately reproduces the slope compared with the data from [43] when ageing temperature is < 810 °C. It is also shown that dependence of the bubble density $N \propto MT[(D^{\text{eff}}(T)/T)t]^{-2/3}$ agrees well with the experiment in the same temperature range < 810 °C.

Measurements were performed in a high homologous temperature range ($> 0.6T_m$), thus, allowing the observation of the growth of bubbles whose sizes are larger than the transition radius (> 50 nm). As well as in the case of 316 steel, the obtained experimental data are compared with theoretical estimates of $R \propto [D_{\text{He}}(T)t]^{1/2}$ and $N \propto MT[D_{\text{He}}(T)t]^{-1}$ for large bubble growth in Cu. It is seen in Figure 3 that the experimental measurements for the highest temperature 920 °C agree well with theoretical predictions.

Table 4. Material parameters for Cu

Parameter	Value	Reference
Amount of helium M , appm	300	[43]
Lattice constant a , Å	3.62	[30]
Atomic volume Ω , m ³	$1.20 \cdot 10^{-29}$	–
Vacancy formation (pre-exponential factor) C_{v0}	5.00	–
Vacancy formation energy E_v^f , eV	1.28	[44]
Vacancy diffusion (pre-exponential factor) D_{v0} , m ² /s	$2.0 \cdot 10^{-5}$	–
Vacancy migration energy E_v^m , eV	0.71	[44]
Helium diffusion (pre-exponential factor) D_{g0} , m ² /s	$5.42 \cdot 10^{-8}$	[45]
Helium migration energy E_g^m , eV	0.117	[45]
Surface energy γ , J/m ²	1.6	[36]
Helium dissociation energy ψ , eV	1.5	–

**Figure 3.** Comparison of the experimental measurements in Cu (black squares indicate data from [43]) with the temperature dependences for R (a) and for N (b) according to the OR model.

Thus, both theoretical dependences provide a good description on evolution of small and larger bubbles over the entire ageing temperature range studied. This shows that bubble growth in Cu actually follows the OR mechanism with a high probability.

4.4. Gas bubble evolution in tungsten

Theoretical dependencies of time and temperature for R and N found in this work are compared with the experimental data for W from [46]. Hot-rolled W samples were implanted with helium by means of homogenous

implantation to 600 appm at 52 °C. The samples were then isochronously annealed for 1 hour in the temperature range from 1200 to 2100 °C. It was found that bubble distributions in W were the same at the grain boundary and within the grain, unlike Ni and Cu. This difference could not be explained unambiguously by the difference in types of atomic structures for metals with BCC and FCC lattices. Analyzing the obtained data, the authors of the experimental study concluded that bubble growth in W followed the BMC mechanism, rather than the OR mechanism.

Material parameters listed in Table 5 were obtained using experimental and mathematical simulation methods.

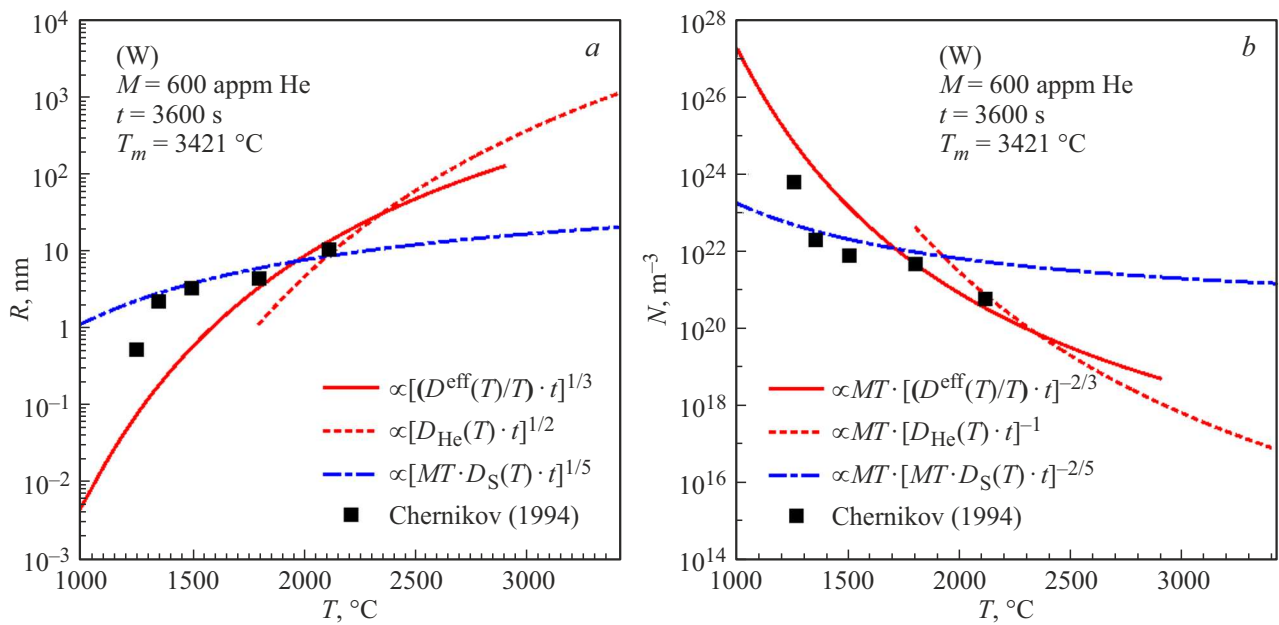


Figure 4. Comparison of the experimental measurements in W (black squares indicate data from [46]) with the temperature dependences for R (a) and for N (b) according to the OR model (solid line, dashed line) and BMC model (dashed-dotted line).

Table 5. Material parameters for tungsten

Parameter	Value	Reference
Amount of implanted helium atoms M , appm	600	[46]
Lattice constant a , Å	3.16	[47]
Atomic volume Ω , m ³	$1.58 \cdot 10^{-29}$	–
Vacancy formation (pre-exponential factor) C_{v0}	1.00	–
Vacancy formation energy E_v^f , eV	3.6	[44]
Vacancy diffusion (pre-exponential factor) D_{v0} , m ² /s	$1 \cdot 10^{-6}$	–
Vacancy migration energy E_v^m , eV	2.26	[48]
Helium atom diffusion (pre-exponential factor) D_{g0} , m ² /s	$5.35 \cdot 10^{-8}$	[45]
Helium migration energy E_g^m , eV	0.13	[45]
Surface energy γ , J/m ²	2.8	[36]
Helium dissociation energy ψ , eV	5.5	–
Surface diffusion (pre-exponential factor) D_{s0} , m ² /s	$1 \cdot 10^{-7}$	–
Surface diffusion (migration energy) E_s , eV	2.26	–

Attempts to find information concerning the energy of helium dissociation from bubbles ψ were not succeeded. For theoretical considerations, a more suitable value is proposed for this parameter: 5.5 eV.

Values of the observed data R and N discovered by the authors of [46] are shown in Figure 4. It also represents theoretical temperature dependences, where helium bubbles grow by the OR mechanism, calculated using the input data given in Table 5. The dependences shown correspondence

to the asymptotic solutions for both small (solid line) and large (dashed line) bubbles. Temperature dependences representing the BMC bubble growth (dashed-dotted line) are also plotted. They were calculated taking into account the same input data given in Table 5 and by using the dependences derived in the work [8].

Assuming that bubble growth follows the OR mechanism, the temperature dependences for R and N (solid and dashed lines) intersect in the point ~ 2350 °C. This intersection is

obtained when ψ was equal to ~ 5.5 eV. Then the transition radius R_{tr} becomes equal to ~ 40 nm, corresponding to those for Ni, Cu and 316 steel.

It is shown that the experimental data for bubbles with the radius < 3 nm at < 1800 °C deviate from the theoretical predictions probably due to the TEM measurement error. Since a significant number of bubbles are not taken into account in the measurements, their observed size is overestimated, and conversely their density is underestimated. Figure 4, *a* shows that the experimental values of R are above the line of theoretical dependence, but the experimental values of N in Figure 4, *b* are below the theoretical curve. This is an expected discrepancy between the experimental measurements and theoretical findings. Under similar conditions, it was also found in Ni and 316 austenitic steel for the corresponding homologous temperatures.

If the parameter ψ is assumed to be equal to ~ 5.5 eV, theoretical temperature dependences $R \propto [(D^{\text{eff}}(T)/T)t]^{1/3}$ and $N \propto MT[(D^{\text{eff}}(T)/T)t]^{-2/3}$ agree well with the experimental data for the two temperatures of 1800 °C and of 2100 °C. At these temperatures, as can be seen in Figure 4, the observed bubble radius does not exceed ~ 10 nm, and bubble density remains high enough $\sim 10^{21} \text{ m}^{-3}$. Thus, the mean bubble radius achieved in W is significantly less than the maximum radius reached in Ni (~ 70 nm), in Cu (~ 200 nm) and in 316 austenitic steel (~ 30 nm). This lack of data for W does not allow us to confirming the applicability of our theory for the annealing temperatures > 2350 °C, when the mean radius R of large bubbles exceeds > 40 nm.

In [46], the authors found that the bubbles in W grow by the BMC mechanism. This can easily be verified by comparing the experimental data and temperature dependences of $R \propto [MT \cdot D_S(T)t]^{1/5}$ and $N \propto MT[MT \cdot D_S(T)t]^{-2/5}$ known from the work [8], where $D_S = D_{S0} \exp(-E_S/k_B T)$ is the diffusion coefficient taken in accordance with the assumption of bubble surface diffusion kinetics. Figure 4 shows that these dependences (dashed-dotted line) are in good agreement with the experimental data in the temperature range from 1300 to 1800 °C. Such the agreement suggests a potential mobility of rather small bubbles in W. On the other hand, it can be seen that in case 1200 °C the observed value of bubble radius R is below the expected dependence, and, on the contrary, the experimental value of bubble density N appears to be above the theoretical curve. Such deviation for bubbles $R < 1$ nm in the lowest annealing temperature point cannot be attributable to the TEM measurement error. Therefore, the conclusion concerning potential mobility of bubble of small sizes $R < 3$ nm is not sufficiently substantiated yet.

Thus, the bubble evolution in W for bubbles with $R > 3$ nm and higher presumably follows the OR mechanism. In order to confirm this assumption, new experimental studies are required, including those of higher (> 2100 °C) annealing temperatures.

5. Conclusion

A new approach based on asymptotic solutions to study helium (monoatomic gas) and hydrogen (diatomic gas) bubble evolution according to the OR mechanism during annealing of irradiated metals has been suggested. Analytical estimations derived on helium bubble evolution have been compared with experimental data for nickel, 316 austenitic stainless steel, copper and tungsten. The comparative analysis of theoretical and experimental data has shown the following:

1. Gas bubble evolution differs at early and later stages of coalescence. Different-sized small and larger bubbles grow at different rates. Nevertheless, asymptotic solutions are identical for monoatomic and polyatomic gases. The solution obtained to the problem of decomposition of two-component gas-vacancy solution appeared to be similar to that given by the LSW theory.

2. Temperature dependences of the mean radius R and density N of rather small sized bubbles, $R < 20\text{--}40$ nm, agree well, in general, with the experimental measurements for all given metals. The smallest bubbles in the range of radii $R < 1\text{--}3$ nm are an exception due to the restrictions caused by the limited TEM resolution.

3. In two cases of 316 austenitic stainless steel and copper, temperature dependences for R and N describe well bubble evolution measured not only at the early, but also at the later stages of coalescence when bubble radius is $R > 20\text{--}40$ nm. Thus, theoretical dependences found for smaller and larger bubbles can explain experimental data in a wide homologous temperature range.

4. Investigation of the experimental data for the given materials has shown that the OR is the most probable bubble growth mechanism during annealing of implanted with helium metals. This is true both for metals with FCC atomic structure (Ni, Cu, 316 austenitic stainless steel) and likely for metals with BCC lattice (W).

Funding

The study was carried out under the state assignment of the National Research Center „Kurchatov Institute“ using the equipment provided by the Shared Research Facility „Complex for Simulation and Processing of Mega-Class Research Facility Data“ NRC „Kurchatov Institute“ <http://ckp.nrcki.ru/>

Conflict of interest

The author declares no conflict of interest.

References

- [1] V.I. Khripunov. VANT. Seriya: Termoyadernyy sintez, **45**, 2, 5 (2022). (in Russian)

- [2] A.I. Blokhin, N.A. Demin, V.M. Tchernov. VANT. Seriya: Materialovedenie i novye materialy **70**, 2006, 108 (2012). (in Russian).
- [3] E.A. Denisov, T.N. Kompaniets, A.A. Yukhimchuk, I.E. Boitsov, I.L. Malkov. Zhurnal tekhnicheskoy fiziki. **83**, 6, 3 (2013).
- [4] S.E. Donnelly. Rad. Eff. **90**, 1 (1985).
- [5] J.B. Condon, T. Schober. J. Nucl. Mater. **207**, 1 (1993).
- [6] G. Greenwood, M. Speight. J. Nucl. Mater. **10**, 140 (1963).
- [7] L.P. Semenov. Atomnaya energiya, **15**(404), (1963). (in Russian).
- [8] S.I. Golubov, R. Stoller, S. Zinkle, A.M. Ovcharenko. J. Nucl. Mater. **361**, 149 (2007).
- [9] A.M. Ovcharenko, I.I. Chernov. J. Nucl. Mater. **528**, 151824 (2020).
- [10] J. Rothaut, H. Schroeder, H. Ullmaier. Philos. Mag. A **47**, 781 (1983).
- [11] Z.K. Saralidze, V.V. Slezov. FTT **7**, 6, 1605 (1965).
- [12] A.J. Markworth. Metall. Trans. **4**, 2651 (1973).
- [13] V.V. Slezov, V.V. Sagalovich. J. Phys. Chem. Solids. **44**, 1, 23 (1983).
- [14] P.G. Cheremskoy, V.V. Slezov, V.I. Betekhtin. Pory v tvoridom tele. Energoatomizdat, M. (1990). s. 102. (in Russian).
- [15] A.M. Ovcharenko, I.I. Chernov, S.I. Golubov. Atomic Energy, **109**, 6, 385 (2011). (Russian Original Atomnaya energiya, **109**, 6, 315 (2010).)
- [16] A.M. Ovcharenko, I.I. Chernov. Atomic Energy, **112**, 5, 360 (2012). (Russian Original Atomnaya energiya **112**, 5, 291 (2012).)
- [17] I.M. Lifshits, V.V. Slezov. ZhETF **35**, 2(8), 479 (1958).
- [18] C. Wagner. Z. Elektrochem. **65**, 581 (1961). (in Russian).
- [19] A.M. Ovcharenko, S.I. Golubov, C.H. Woo, H. Hanchen. Comp. Phys. Comm. **152**, 208 (2003).
- [20] R. Wagner, R. Kampmann, P.W. Voorhees. Phase Transformations in Materials. Ed. Gernot Kostorz. WILEY-VCH Verlag GmbH, Weinheim (2001). P. 309.
- [21] S.A. Kukushkin, A.V. Osipov. ZhETF **113**, 6, 2193 (1998). (in Russian).
- [22] B.V. Kuteev, V.S. Petrov, Yu.S. Shpansky, A.V. Klishchenko. Patent RU127992U1 (2013).
- [23] Ya.B. Zeldovich. ZhETF, **12**, (525), 1942 (2002). (in Russian).
- [24] C.F. Clement, M.H. Wood. Proc. R. Soc. London A **371**, 553 (1980).
- [25] F.C. Goodrich, Proc. R. Soc. London A **277**, 167 (1964).
- [26] V.A. Pechenkin, Yu.V. Konobeev. VANT. Seriya: RP and RM **1**, 6, 8 (1978).
- [27] Yu.V. Konobeev, S.I. Golubov, V.A. Pechenkin. VANT. Seriya: FRP and RM **3**, 17, 44 (1981).
- [28] V.N. Chernikov, H. Trinkaus, P. Jung, H. Ullmaier. J. Nucl. Mater. **170**, 31 (1990).
- [29] J. Laakmann. Berichte der Kernforschungsanlage Jülich, J L-2007, ISSN 03660885 (1985).
- [30] W.G. Wolfer, A. Si-Ahmed. J. Nucl. Mater. **99**, 1, 117 (1981).
- [31] H. Wiedersich, B.O. Hall. J. Nucl. Mater. **66**, 187 (1977).
- [32] A. Seeger, H. Mehrer. Vacancies and interstitials in metals. Ed. by A. Seeger, D. Schumacher, W. Schilling, J. Diehl. North Holland, Amsterdam. (1970).
- [33] K. Maier, H. Mehrer, E. Lessmann, W. Schule. Phys. Stat. Sol. B **78**, 689 (1976).
- [34] V. Philipps, K. Sonnenberg, J.M. Williams. J. Nucl. Mater. **107**, 271 (1982).
- [35] W.D. Wilson, R.A. Johnson. Interatomic potentials and simulation of lattice defects, Eds. C. Gehlen, J.R. Beeler, R.I. Jaffee, Plenum, N.Y. (1972). P. 375. (in Russian).
- [36] W.R. Tyson. Can. Metall. Q. **14**, 4, 307 (1975).
- [37] I. Villacampa, J.C. Chen, P. Spätig, H.P. Seifert, F. Duval. J. Nucl. Mater. **500**, 389 (2018).
- [38] H. Shinno, H. Shiraishi, R. Watanabe, H. Kamitsubo, I. Kohno, T. Shikata. J. Nucl. Mater. **97**, 291 (1981).
- [39] M.R. Hayns, J. Gallagher, R. Bullough. J. Nucl. Mater. **78**, 236 (1978).
- [40] R.E. Stoller, G.R. Odette. ASTM STP 995 (1987). P. 371.
- [41] M.J. Makin, G.P. Walters, A.J.E. Foreman. J. Nucl. Mater. **95**, 155 (1980).
- [42] D.J. Reed. Radiat. Eff. **31**, 129 (1977).
- [43] V.N. Chernikov. J. Nucl. Mater. **195**, 29 (1992).
- [44] J.A. Ytterhus, R.W. Balluffi. Phil. Mag. **11**, 112, 707 (1965).
- [45] M. Li, Q. Hou, J. Cui, M. Qiu, A. Yang, B. Fu. Nuclear Inst. Meth. Phys. Res. B **463**, 30 (2020).
- [46] V.N. Chernikov, Ju.V. Lakhotkin, H. Ullmaier, H. Trinkaus, P. Jung, H.J. Bierfeld. J. Nucl. Mater. **212–215**, 375 (1994).
- [47] F.H. Featherston, J.R. Neighbours. Phys. Rev. **130**, 4, 1324 (1963).
- [48] P.J. Wynblatt. J. Phys. Chem. Solids **29**, 2, 215 (1968).

Translated by E.Ilinskaya